

Omnipose: a high-precision morphology-independent solution for bacterial cell segmentation

Kevin J. Cutler¹, Carsen Stringer², Paul A. Wiggins^{1,3,*} and Joseph D. Mougous^{4,5,*}

¹Department of Physics, University of Washington, Seattle, WA 98195, USA

²HHMI Janelia Research Campus, Ashburn, VA, USA

³Department of Bioengineering, University of Washington, Seattle, WA 98195, USA

⁴Department of Microbiology, University of Washington, Seattle, WA 98109, USA

⁵Howard Hughes Medical Institute, University of Washington, Seattle, WA 98195, USA

* To whom correspondence should be addressed:

Email – pwiggins@uw.edu, mougous@uw.edu

1 **Abstract**

2 Advances in microscopy hold great promise for allowing quantitative and precise
3 readouts of morphological and molecular phenomena at the single cell level in bacteria.
4 However, the potential of this approach is ultimately limited by the availability of
5 methods to perform unbiased cell segmentation, defined as the ability to faithfully
6 identify cells independent of their morphology or optical characteristics. In this study, we
7 present a new algorithm, Omnipose, which accurately segments samples that present
8 significant challenges to current algorithms, including mixed bacterial cultures,
9 antibiotic-treated cells, and cells of extended or branched morphology. We show that
10 Omnipose achieves generality and performance beyond leading algorithms and its
11 predecessor, Cellpose, by virtue of unique neural network outputs such as the gradient of
12 the distance field. Finally, we demonstrate the utility of Omnipose in the context of
13 characterizing extreme morphological phenotypes that arise during interbacterial
14 antagonism. Our results distinguish Omnipose as a uniquely powerful tool for answering
15 diverse questions in bacterial cell biology.

16 **Introduction**

17 Although light microscopy is a valuable tool for characterizing cellular and sub-
18 cellular structures and dynamics, quantitative analysis of microscopic data remains a
19 persistent challenge (1). This is especially pertinent to the study of bacteria, many of
20 which have dimensions in the range of optical wavelengths. Thus, their cell body is
21 composed of a small number of pixels (*e.g.*, $\sim 100\text{-}300 \text{ px}^2$ for *E. coli* at 100x
22 magnification). At this scale, accurate subcellular localization requires defining the cell
23 boundary with single-pixel precision. The process of defining cell boundaries within
24 micrographs is termed cell segmentation and this is a critical first step in current image
25 analysis pipelines (2, 3).

26 In addition to their small size, bacteria adopt a wide range of morphologies.
27 Although many commonly studied bacteria are well-approximated by idealized rods or
28 spheres, there is growing interest in bacteria with more elaborate shapes (4). Some
29 examples include Streptomyetales, which form long filamentous and branched hyphal
30 structures (5), and Caulobacterales, which generate extended appendages distinct from
31 their cytoplasm (6). Furthermore, microfluidic devices are allowing researchers to capture
32 the responses of bacteria to assorted treatments such as antibiotics, which often result in
33 highly irregular morphologies (7). Whether native or induced, atypical cell morphologies
34 present a distinct problem at the cell segmentation phase of image analysis (8, 9). This is
35 compounded when such cells are present with those adopting other morphologies, as is
36 the case in many natural samples of interest (10). To date, there are no solutions for
37 segmenting bacterial cells of assorted shape and size in a generalizable manner (1).

38 Cell segmentation is a complex problem that extends beyond microbiological
39 research, thus many solutions are currently available in image analysis programs (8, 9,
40 11-27). Most of these solutions use traditional image processing techniques such as the
41 application of an intensity threshold to segment isolated cells; however, this approach
42 does not perform well for cells in close contact and it requires extensive parameter-tuning
43 in order to optimize for a given cell type. SuperSegger was developed to address these
44 issues specifically in bacterial phase contrast images (13). This program utilizes both
45 traditional image filtering techniques and a shallow neural network to correct for errors
46 that thresholding and watershed segmentation tend to produce.

47 Deep neural networks (DNNs) are now widely recognized as superior tools for
48 cell segmentation (28). Unlike traditional image processing, machine-learning approaches
49 such as DNNs require training on a ground-truth dataset of cells and corresponding
50 labels. Trained DNNs are thus limited in applicability to images that are representative of
51 those in the training dataset. Early DNN approaches were based on the Mask R-CNN
52 architecture (24), whereas more recent algorithms such as StarDist, Cellpose, and MiSiC
53 are based on the U-Net architecture (12, 15, 26). Pachitariu and colleagues showed that
54 Cellpose outperforms Mask R-CNN and StarDist on a variety of cell types and cell-like
55 objects, distinguishing it as a general solution for cell segmentation (12). Notably, the
56 representation of bacteria in their study was limited. MiSiC was developed as a general
57 DNN-based solution for bacterial segmentation; however, the authors of MiSiC did not
58 provide comparisons to other DNN algorithms (15). Here, we evaluated the performance
59 of state-of-the-art cell segmentation algorithms on a diverse collection of bacterial cells.
60 Our findings motivated the design of a new algorithm, Omnipose, that significantly

61 outperforms all previous cell segmentation algorithms across a wide range of bacterial
62 cell sizes, morphologies, and optical characteristics. We have made Omnipose and all
63 associated data immediately available to researchers, and we anticipate that our model –
64 without retraining – can be applied to diverse bacteriological systems. Furthermore,
65 following the incorporation of additional ground truth data, Omnipose could serve as a
66 platform for segmenting various eukaryotic cells and extended, anisotropic objects more
67 broadly.

68

69 **Results**

70 **Evaluation of bacterial cell segmentation algorithms**

71 Numerous image segmentation algorithms have been developed, and the
72 performance of many of these on bacterial cells is documented (1). These broadly fall
73 into three categories: (i) traditional image processing approaches (*e.g.*, thresholding,
74 watershed), (ii) traditional/machine learning hybrid approaches, and (iii) deep neural
75 network (DNN) approaches. Given the goal of developing software with the capacity to
76 recognize bacteria universally, we sought to identify strongly performing algorithms for
77 further development. An unbiased, quantitative comparison of cell segmentation
78 algorithms on bacterial cells has not been performed; thus, we selected one or more
79 representatives from each category for our analysis: Morphometrics (23) (i), SuperSegger
80 (13) (ii), Mask R-CNN (27), StarDist (26), MiSiC (15), and Cellpose (12) (iii). For a
81 detailed review of these choices, see Methods.

82 For training and benchmarking these algorithms, we acquired micrographs of
83 assorted bacterial species representing diverse morphologies and optical characteristics.

84 Many studies of bacteria involve mutations or treatments that cause extreme
85 morphologies. To capture this additional diversity, we included wild-type and mutant
86 bacteria grown in the presence of two beta-lactam antibiotics, cephalexin and aztreonam,
87 and A22, which targets MreB (29). Finally, based on our interest in microbial
88 communities, we acquired images of mixtures of bacteria which display distinct
89 morphologies and optical characteristics. In total, we collected 4833 images constituting
90 approximately 700,900 individual cells deriving from 14 species (Table S1). Next, we
91 developed a streamlined approach for manual cell annotation and applied it to these
92 images (see Methods), yielding 46,000 representative annotated cells that serve as our
93 ground-truth dataset. We arbitrarily split this data into a 27,000-cell training set and a
94 19,000-cell benchmarking set. Relevant cellular metrics did not differ substantially
95 between the groups, confirming that the benchmarking set faithfully represents the
96 training set (Fig. S1).

97 To facilitate direct comparison of the algorithms, we first optimized their
98 performance against our data. For the DNN approaches, each algorithm was trained on
99 our dataset using developer-recommended parameters. Morphometrics and SuperSegger
100 cannot be automatically optimized using ground-truth data; therefore, we manually
101 identified settings that optimized the performance of these algorithms against our dataset
102 (see Methods). As a quantitative measure for algorithm performance, we compared their
103 average Jaccard Index (JI) as a function of intersection over union (IoU) threshold – a
104 well-documented approach for evaluating image segmentation (Fig. 1A) (30, 31). IoU
105 values lie between zero and one, with values greater than 0.8 marking the point at which
106 masks become indistinguishable from ground truth by the expert human eye (Fig. S2)

107 (30). This analysis showed that DNN-based approaches significantly outperform other
108 algorithms. However, within the DNN group, substantial differences in performance were
109 observed; Cellpose and StarDist outperform Mask R-CNN and MiSiC at high IoU
110 thresholds. The performance of all algorithms varied greatly across the images in our
111 ground-truth dataset, with much of this variability delineated by cell type and
112 morphology categories (Fig. 1B-G). Whereas all other algorithms exhibited visible
113 segmentation errors in two of the three cell categories we defined, errors by Cellpose –
114 the best overall performing algorithm at high IoU thresholds – were only apparent in
115 elongated cells (Fig. 1H-J).

116

117 **Motivation for a new DNN-based segmentation algorithm**

118 Our comparison revealed that Cellpose offers superior performance relative to the
119 other segmentation algorithms we analyzed, and for this reason, we selected this
120 algorithm for further development. Notably, even at the high performance levels of
121 Cellpose, only 83% of predictions on our benchmarking dataset are above 0.8 IoU. This
122 limits the feasibility of highly quantitative studies such as those involving subcellular
123 protein localization or cell–cell interactions.

124 Cellpose utilizes a neural network that is trained on ground-truth examples to
125 transform an input image into several intermediate outputs, including a scalar probability
126 field for identifying cell pixels (Fig. S3A, panels *i-iii*) (12). Cellpose is unique among
127 DNN algorithms by the addition of a vector field output, which is defined by the
128 normalized gradient of a heat distribution from the median cell pixel coordinate (Fig.
129 S3A, panels *iv,v*). This vector field directs pixels toward a global cell center via Euler

130 integration, allowing cells to be segmented based on the points at which pixels coalesce
131 (Fig. S3B). In contrast to other algorithms, this approach for reconstructing cells is size-
132 and morphology-independent, insofar as the cell center can be correctly defined.

133 To further interrogate the accuracy of Cellpose on our dataset, we evaluated its
134 performance as a function of cell size. We compared cell area against the number of
135 segmentation errors, calculated as the number of redundant or missing masks
136 corresponding to each ground-truth cell mask. This revealed a strong correlation between
137 cell size and segmentation errors, with the top quartile of cells accounting for 83% of all
138 errors (Fig. 2A). To understand the source of these errors, we inspected the flow field
139 output of many poorly segmented cells across a variety of species and growth conditions.
140 This showed that elongated cells, an important morphology often seen in both wild-type
141 and mutant bacterial populations, are particularly susceptible to over-segmentation (Fig.
142 2B). We attribute this to the multiple sinks apparent in the corresponding flow fields. In
143 the Cellpose mask reconstruction algorithm, pixels belonging to these cells are guided
144 into multiple centers per cell, fragmenting the cell into many separate masks.

145 We hypothesized that the observed defect in Cellpose flow field output is a
146 consequence of two distinct flow field types arising from our training dataset: those
147 where the median pixel coordinate, or ‘center’, lies within the cell (97.8%) and those
148 where it lies outside the cell (2.2%). In the latter, Cellpose projects the center point to the
149 nearest boundary pixel, ultimately leading to points of negative divergence on the cell
150 periphery that are chaotically distributed (Fig. 2C-E). On the contrary, non-projected
151 centers maintain a uniform field magnitude along the entire boundary and adhere to the
152 global symmetries of the cell (Fig S4A,D). A similar issue is also encountered in cells

153 with centers that are not projected but lie close to the boundary (Fig. S4B-D). Cells with a
154 center point closer than 0.3 times the mean cell diameter (a factor of 0.2 off-center) to the
155 boundary account for an additional 8.5% of our data. Neural networks can be exquisitely
156 sensitive to the outliers in their training data (32); therefore, we suspect that this small
157 fraction of corrupt flow fields has significantly impacted the performance of Cellpose.

158

159 **Development of a new DNN-based segmentation algorithm**

160 As there exists no straightforward means of defining a cell center for irregular
161 objects, we sought to develop a segmentation algorithm that operates independently of
162 cell center identification. We built our new algorithm, which we named Omnipose,
163 around the scalar potential known as the distance field (or distance transform), which
164 describes the distance at any point \vec{x} in a bounded region Ω to the closest point on the
165 boundary $\partial\Omega$. Notably, this widely utilized construct is one of the intermediate outputs of
166 StarDist (32). Whereas in StarDist it is used to seed and assemble star-convex polygons,
167 its use in Omnipose is to define a new flow field within the Cellpose framework. The use
168 of a distance field has several advantages. First, the distance field is defined by the
169 eikonal equation $|\vec{\nabla}\Phi(\vec{x})| = 1$, and so its gradient has unit magnitude throughout the
170 bounded region for which it is calculated. This grants it faster convergence and better
171 numerical stability when compared to alternative solutions producing similar fields (*e.g.*,
172 screened Poisson; see Methods) (Figure S5A). Second, the distance field is independent
173 of morphology and topology, meaning that it is applicable to all cells. Lastly, the
174 resulting flow field points uniformly from cell boundaries toward the local cell center,
175 coinciding with the medial axis, or skeleton, that is defined by the stationary points of the

176 distance field (Figure S5B). This critical feature allows pixels to remain spatially
177 clustered after Euler integration, solving the problem of over-segmentation seen in
178 Cellpose.

179 One challenge to using the distance field as the basis to our approach is that
180 traditional distance field algorithms like FMM (Fast Marching Method) are sensitive to
181 boundary pixilation (33), causing artifacts in the flow field that extend deep into the cell.
182 These artifacts are sensitive to pixel-scale changes at the cell perimeter, which we
183 reasoned would interfere with the training process. To solve this, we developed an
184 alternative approach based on FIM (Fast Iterative Method) that produces smooth distance
185 fields for arbitrary cell shapes and sizes (Fig. 3A, and see Methods) (34). The
186 corresponding flow field is relatively insensitive to boundary features at points removed
187 from the cell boundary, a critical property for robust and generalized prediction by the
188 Cellpose network.

189 The use of the distance field additionally required a unique solution for mask
190 reconstruction. Whereas the pixels in a center-seeking field converge on a point, standard
191 Euler integration under our distance-derived field tends to cluster pixels into multiple thin
192 fragments along the skeleton, causing over-segmentation (Fig. 3B). We solved this with a
193 suppression factor of $(t + 1)^{-1}$ in each time step of the Euler integration. This reduces
194 the movement of each pixel after the first step $t = 0$, facilitating initial cell separation
195 while preventing pixels from clustering into a fragmented skeleton formation. The wider
196 distribution resulting from our suppression factor allows pixels to remain connected,
197 thereby generating a single mask for each cell in conjunction with a standard automated
198 pixel clustering algorithm (*e.g.*, DBSCAN) (35).

199

200 **Omnipose demonstrates unprecedented segmentation accuracy of bacterial cells**

201 With solutions to the major challenges of cell center-independent segmentation
202 incorporated into Omnipose, we proceeded to benchmark its performance. Remarkably,
203 across the IoU threshold range 0.5-1.0, Omnipose averages a JI >10-fold above that of
204 Cellpose (Fig. 4A). The difference in performance between the algorithms is particularly
205 pronounced within the high IoU range (0.75-1.0), where we observe an average of 170-
206 fold higher JI for Omnipose. At the 0.5-5 μm scale and with a typical microscope
207 configuration, quantitative measurements rely upon IoU values in this range, thus
208 Omnipose is uniquely suited for the microscopic analysis of bacterial cells.

209 To dissect the contributions of the individual Omnipose innovations to the overall
210 performance of the algorithm, we isolated the mask reconstruction component of
211 Omnipose and applied it to the Cellpose network output. This augmentation of Cellpose
212 modestly improved its performance to a roughly equivalent extent across all IoU
213 thresholds (Fig. 4A). Based on this, we attribute the remaining gains in performance by
214 Omnipose to its unique network outputs and our improvements to the Cellpose training
215 framework (see Methods).

216 Our analyses illuminated critical flaws in prior DNN-based approaches for the
217 segmentation of elongated cells, effectively preventing these algorithms from
218 generalizable application to bacteria (Fig. 1). To determine whether Omnipose overcomes
219 this limitation, we evaluated its performance as a function of cell area. Cell area serves as
220 a convenient proxy for cell length in our dataset, which is composed of both branched
221 and unbranched elongated cells. Whereas the Cellpose cell error rate remains above 9%

222 and increases exponentially with cell size, Omnipose displays a consistent error rate that
223 remains below 4% for all percentiles (Fig. 4B). Thus, Omnipose performance is
224 independent of cell size and shape, including those cells with complex, extended
225 morphologies (Fig. 4C,D).

226

227 **Omnipose permits sensitive detection of cellular intoxication**

228 Our laboratory recently described an interbacterial type VI secretion system-
229 delivered toxin produced by *Serratia proteamaculans*, Tre1 (36). We showed that this
230 toxin acts by ADP-ribosylating the essential cell division factor FtsZ; however, we were
231 unable to robustly evaluate the consequences of Tre1 intoxication on target cell
232 morphology owing to segmentation challenges. Here we asked whether Omnipose could
233 permit straightforward and sensitive detection of intoxication by Tre1. To this end, we
234 incubated *S. proteamaculans* wild-type or a control strain expressing inactive Tre1
235 (*tre1^{E415Q}*) with target *E. coli* cells and imaged these mixtures after a fixed period of 20
236 hours. Owing to the unique capabilities of Omnipose, we were able to include dense
237 fields of view, incorporating >300,000 cells in our analysis.

238 Among the cells identified by Omnipose, we found a small proportion were
239 elongated and much larger than typical bacteria (Fig. 5A,B and Fig. S6A). These cells
240 were only detected in mixtures containing active Tre1, and the apparent failure of the
241 cells to septate is consistent with the known FtsZ-inhibitory activity of the toxin. The *S.*
242 *proteamaculans* strain background we employed in this work expresses the green
243 fluorescent protein. Corresponding fluorescence images allowed us to unambiguously
244 assign the enlarged cell population to *E. coli* (Fig. 5C). Next, we subjected the same

245 images to cell segmentation with StarDist, Cellpose, and MiSiC, the three top-performing
246 algorithms in our initial survey. Each of these algorithms fail to identify this population
247 of cells to high precision (Fig. 5D,E). Close inspection reveals three distinct modes of
248 failure (Fig. 5E and Fig. S6B). In the case of StarDist, elongated (non-star-convex) cells
249 are split into multiple star-convex subsets that do not span the entire cell. Cellpose detects
250 entire elongated cells, but it breaks them up into a multitude of smaller masks.
251 Conversely, MiSiC detects all cells but fails to properly separate them, making the area
252 measurement exaggerated in many cases. Taken together, these data illustrate how the
253 enhanced cell segmentation performance of Omnipose can facilitate unique insights into
254 microbiological systems.

255

256 **Discussion**

257 Confronted with the importance of segmentation accuracy to the success of work
258 within our own laboratory, we were motivated to characterize the performance of several
259 existing cell segmentation algorithms. Recent developments in deep learning have greatly
260 improved these algorithms; however, significant challenges remain (1, 30). Although
261 isolated cells without cell-to-cell contact can be segmented with high precision by any of
262 the packages we tested, segmentation becomes significantly more challenging when cells
263 form microcolonies, adopt irregular morphologies, or when fields are composed of cells
264 with multiple shapes and sizes. Such difficulties are compounded in time-lapse studies,
265 where the significance of segmentation errors often grows exponentially with time.
266 Experimental design can help mitigate certain segmentation challenges; however, the

267 recent emphasis on non-model organisms and microbial communities renders this an
268 increasingly undesirable solution (37).

269 This work provides the most comprehensive side-by-side quantitative comparison
270 of cell segmentation algorithm performance to-date. As expected, machine-learning-
271 based approaches outperform others, yet insights into general image segmentation
272 strategies can be gained from each of the methods we examined. Two of the six
273 algorithms we tested utilize traditional image thresholding and watershed segmentation:
274 Morphometrics and SuperSegger (13, 23). Each program tends to under-segment adjacent
275 cells and over-segment large cells, behaviors previously linked to thresholding and
276 watershed processes, respectively (1, 38). Given that SuperSegger was motivated at least
277 in-part to mitigate these issues, we postulate that traditional image segmentation
278 approaches are ultimately limited to specialized imaging scenarios. Although we classify
279 MiSiC as a DNN-based approach, this algorithm also relies on thresholding and
280 watershed segmentation to generate cell masks from its network output (15). The network
281 output of MiSiC is more uniform than unfiltered phase contrast images, yet this pre-
282 processing does not fully abrogate the typical errors of thresholding and watershed
283 segmentation. We therefore conclude that, even when combined with neural networks as
284 seen in MiSiC, thresholding and watershed cannot be effectively used for general cell
285 segmentation tasks.

286 A successful DNN-based algorithm is composed of a robust, consistent neural
287 network output, and an appropriate mask reconstruction process based on this output. In
288 the case of Mask R-CNN, bounding boxes for each cell are predicted along with a
289 probability field that localizes a cell within its bounding box (39). Masks are generated

290 by iterating over each box and thresholding the probability field. Despite the widespread
291 adoption of Mask R-CNN, we found this algorithm did not perform exceptionally well in
292 our study. Our results suggest that this is due to dense cell fields with overlapping
293 bounding boxes, a feature known to corrupt the training process and produce poor
294 network outputs for Mask R-CNN (40). By contrast, the StarDist network makes robust
295 predictions, but it fails to assemble accurate cell masks because the cells in our dataset
296 are not well approximated by star-convex polygons (26). The errors we encountered with
297 Cellpose can be attributed to both neural network output and mask reconstruction. In
298 Omnipose, we specifically addressed these two issues via the distance field and
299 suppressed Euler integration, respectively, yielding a remarkably precise and
300 generalizable image segmentation tool. Omnipose effectively leverages the strongest
301 features of several of the DNN approaches we tested, namely the distance field of
302 StarDist, the boundary field of MiSiC, and the mask reconstruction framework of
303 Cellpose.

304 We have designed Omnipose for use by typical research laboratories and we have
305 made its source code and training data publicly available. For images of bacteria under
306 phase contrast, researchers will not need to provide new ground truth data or retrain the
307 model. In this study, we emphasized morphological diversity, but we further accounted
308 for differences in optical features between bacterial strains, slide preparation techniques,
309 and microscope configurations. For example, the images in our ground-truth dataset
310 originate from four different researchers using distinct microscopes, objectives, sensors,
311 illumination sources, and acquisition settings. We further introduced extensive test-time
312 augmentations that simulate variations in image intensity, noise, gamma, clipping, and

313 magnification. Lastly, bacterial strains exhibit a wide range of intrinsic contrast and
314 internal structure, often exacerbated by antibiotic treatment or revealed by dense cell
315 packing. Internal structure can cause over-segmentation, so we included many cells with
316 this characteristic in our dataset.

317 Although we have highlighted the utility of Omnipose in the context of bacterial
318 phase contrast images, it can also be used to segment a variety of cells (or cell-like
319 objects) captured with one or multiple imaging modalities. The cyto2 dataset of Cellpose
320 consists of a large set of user-submitted images and corresponding ground-truth
321 annotations, which we used to train a separate Omnipose model (12, 30). Despite modest
322 improvements in speed and accuracy relative to Cellpose, we note that the absolute
323 performance of Omnipose on the cyto2 dataset is lower than what we obtained on our
324 bacterial dataset (Fig. S7). We reason that two variables may account for this
325 discrepancy. First, the cyto2 dataset is sourced from many contributors, such that
326 consistency and quality of annotation cannot be verified. Second, although our bacterial
327 dataset is quite diverse, it is uniform relative to the tremendous diversity of images
328 present in the cyto2 dataset (*e.g.*, apples, seashells, plant cells, animal cells, etc.). We
329 therefore postulate that domain and modality uniformity is required to replicate our
330 results with Omnipose on non-bacterial datasets.

331 We anticipate that the unprecedented performance of Omnipose may permit
332 access to information from microscopy images that was previously inaccessible. For
333 instance, images deriving from natural microbial communities could be accurately
334 characterized with regard to internal structure, autofluorescence, and morphology at the
335 single-cell level. This data could be used to estimate diversity, a novel methodology that

336 would complement existing sequencing-based metrics (41). It is worth noting that
337 phenotypic diversity often exceeds genetic diversity (42); therefore, even in a relatively
338 homogeneous collection of organisms, precise segmentation could allow classes
339 representing distinct states to be identified. A microscopy-based approach also offers the
340 opportunity to characterize spatial relationships between cells, information that is
341 exceptionally difficult to recover in most biomolecular assays.

342 **Methods**

343 **Phase contrast and fluorescence microscopy**

344 In-house imaging was performed on a Nikon Eclipse Ti-E wide-field epi-
345 fluorescence microscope, equipped with a sCMOS camera (Hamamatsu) and X-cite LED
346 for fluorescence imaging. We imaged through 60X and 100X 1.4 NA oil-immersion PH3
347 objectives. The microscope was controlled by NIS-Elements. Cell samples were spotted
348 on a 3% (w/v) agarose pad placed on a microscope slide. The microscope chamber was
349 heated to 30°C or 37°C when needed for time-lapse experiments.

350 Several images in our dataset were taken by two other laboratories using three
351 distinct microscope/camera configurations. The Brun lab provided images of *C.*
352 *crescentus* acquired on a Nikon Ti-E microscope equipped with a Photometrics Prime
353 95B sCMOS camera. Images were captured through a 60X Plan Apo λ 100X 1.45 NA oil
354 Ph3 DM objective. The Wiggins lab provided *E. coli* and *A. baylyi* time lapses from both
355 a Nikon Ti-E microscope as well as a custom-built tabletop microscope, both described in
356 previous studies (43, 44).

357

358 **Sample preparation**

359 To image antibiotic-induced phenotypes, cells were grown without antibiotics
360 overnight in LB, back-diluted, and spotted on agarose pads with 50 μ g/mL A22 or
361 10 μ g/mL cephalixin. Time lapses were captured of *E. coli* DH5 α and *S. flexneri* M90T
362 growing on these pads. *E. coli* CS703-1 was back-diluted into LB containing 1 μ g/mL
363 aztreonam and spotted onto a pad without antibiotics (45). Cells constitutively expressed
364 GFP to visualize cell boundaries.

365 *H. pylori* LSH100 grown with and without Aztreonam was provided by the
366 Salama lab (46, 47). Samples were fixed and stained with Alexafluor 488 to visualize the
367 cell membrane. Images were taken on LB pads. The typical technique of allowing the
368 spot to dry on the pad caused cells to curl up on themselves, so our images were taken by
369 placing the cover slip on the pad immediately after spotting and applying pressure to
370 force out excess media.

371 *C. crescentus* was cultivated and imaged by the Brun lab (48, 49). Cells were
372 grown in PYE, washed twice in water prior to 1:20 dilution in Hutner base-imidazole-
373 buffered-glucose-glutamate (HIGG media) and grown at 26°C for 72h. Cells were spotted
374 on a 1% agarose PYE pads prior to imaging.

375 *S. pristinaespiralis* NRRL 2958 was grown using the following media recipe:
376 Yeast extract 4g/L, Malt extract 10g/L, Dextrose 4g/L, Agar 20g/L. This media was used
377 to first culture the bacteria in liquid overnight and then on a pad under the microscope.
378 This strain forms aggregates in liquid media, so these aggregates were allowed to grow
379 for several hours on a slide in the heated microscope chamber until we could see
380 individual filaments extending from the aggregates. Fields of view were selected and
381 cropped to exclude cell overlaps. Autofluorescence was captured to aid in manual
382 segmentation.

383 Mixtures of *S. proteamaculans* attTn7::Km-gfp *treI* or *treI*^{E415Q} and *E. coli* were
384 spotted on a PBS pad to prevent further growth. Phase-contrast images of the cells were
385 acquired before and after a 20hr competition on a high-salt LB plate. Fluorescence
386 images in the GFP channel were also acquired to distinguish *S. proteamaculans* from
387 unlabeled *E. coli*.

388 All other individual strains in Table S1 were grown overnight, diluted 1:100 into
389 fresh LB media, and grown for 1-3 hours before imaging. Mixtures were made by
390 combining back-diluted cells roughly 1:1 by OD₆₀₀.

391

392 **Manual cell annotation**

393 Manual annotation began with loading the images into MATLAB, normalizing
394 the channels, registering the fluorescence channel(s) to phase (when applicable), and
395 producing boundary-enhanced versions of phase and fluorescence. Where possible,
396 fluorescence data was primarily used to define cell boundaries. In addition to a blank
397 channel to store manual labels, all processed phase and fluorescence images were then
398 automatically loaded as layers into an Adobe Photoshop document. We used 4-6 unique
399 colors and the Pencil tool (for pixel-level accuracy and no blending) to manually define
400 cell masks. Due to the 4-color theorem (50), this limited palette was sufficient to clearly
401 distinguish individual cells from each other during annotation. This color simplification is
402 not found in any segmentation GUI, and it enabled faster manual annotation by reducing
403 the need to select new colors. It also eliminated the confusion caused by the use of
404 similar but distinct colors in adjacent regions, which we suspect is the principal cause for
405 the misplaced mask pixels that we observed in other datasets (*e.g.*, cyto2).

406 The cell label layer was then exported as a PNG from Photoshop, read back into
407 MATLAB, and converted from the repeating N-color labels to a standard 16-bit integer
408 label matrix, where each cell is assigned a unique integer from 1 to the number of cells
409 (background is 0). Because integer labels cannot be interpolated, we then performed a
410 non-rigid image registration of the phase contrast channel to the binary label mask to

411 achieve better phase correlation to ground truth masks. All images in our ground-truth
412 dataset have been registered in this manner.

413

414 **Choosing Segmentation algorithms**

415 Three main factors contributed to the choice of algorithms highlighted in this
416 study: (i) specificity to bacterial phase contrast images, (ii) success and community
417 adoption, especially for bioimage segmentation, and (iii) feasibility of installation,
418 training, and use. SuperSegger, Morphometrics, and MiSiC were selected because they
419 specifically targeted the problem of bacterial phase contrast segmentation (15, 23, 51).
420 Packages such as BactMAP, BacStalk, Cellprofiler, CellShape, ColiCoords, Cytokit,
421 MicroAnalyzer, MicrobeJ, Oufiti, and Schnitzcells incorporate limited novel segmentation
422 solutions and instead aim to provide tools for single-cell analysis such as lineage tracing
423 and protein tracking (8, 9, 14, 18-20, 25, 52-54). Furthermore, the segmentation that these
424 programs perform depends broadly on thresholding and watershed techniques; therefore,
425 Morphometrics is a reasonable proxy for their segmentation capabilities. We were unable
426 to locate code or training data for BASCA (11). Ilastik is a popular interactive machine-
427 learning tool for bioimage segmentation, but training it using a manual interface was not
428 feasible on a large and diverse dataset such as our own (21). Among DNN approaches,
429 Mask R-CNN was selected because it is a popular architecture for handling typical image
430 segmentation tasks. It was also used in the segmentation and tracking package Usiigaci
431 (24). U-Net architectures have been implemented in a number of algorithms, including
432 DeLTA, PlantSeg, MiSiC, StarDist, and Cellpose (12, 15, 17, 22, 26). DeLTA was not
433 included in this study because it operates similarly to MiSiC and was designed

434 specifically for mother machine microfluidics analysis. DeLTA 2.0 was recently released
435 to additionally segment confluent cell growth on agarose pads, but it remains quite
436 similar to MiSiC in implementation (55). PlantSeg could, in principle, be trained on
437 bacterial micrographs, but we determined that its edge-focused design meant to segment
438 bright plant cell wall features would not offer any advancements over the remaining U-
439 Net methods that we tested.

440

441 **Training and tuning segmentation algorithms**

442 All segmentation algorithms have tunable parameters to optimize performance on
443 a given dataset. These include pre-processing such as image rescaling (often to put cells
444 into a particular pixel diameter range), contrast adjustment, smoothing, and noise
445 addition. Morphometrics and SuperSegger were manually tuned to give the best results
446 on our benchmarking dataset. The neural network component of SuperSegger was not
447 retrained on our data, as this is a heavily manual process involving toggling watershed
448 lines on numerous segmentation examples. DNN-based algorithms are automatically
449 trained using our dataset, and the scripts we used to do so are available in our GitHub
450 repository. We adapted our data for MiSiC by transforming our instance labels into
451 interior and boundary masks. Training documentation for MiSiC is not published, but our
452 training and evaluation parameters were tuned according to correspondence with the
453 MiSiC authors. Cellpose and StarDist were trained with the parameters provided in their
454 excellent documentation. StarDist has an additional tool to optimize image pre-
455 processing parameters on our dataset, which we utilized.

456

457 **Evaluating segmentation algorithms**

458 All algorithms were evaluated on our benchmarking dataset with manually or
459 automatically optimized parameters. We provide both the raw segmentation results for all
460 test images by each tested algorithm as well as the models and model-training scripts
461 required to reproduce our results. Before evaluating IoU or JI, small masks at image
462 boundaries were removed for both the ground-truth and predicted masks. IoU and JI are
463 calculated on a per-image basis and, where shown, are averaged with equal weighting
464 over the image set or field of view.

465 Our new metric, the number of segmentation errors per cell, was calculated by
466 first measuring the fraction of each predicted cell that overlaps with each ground truth
467 cell. A predicted cell is assigned to a ground-truth cell if the overlap ratio is ≥ 0.75 ,
468 meaning that at least three quarters of the predicted cell lies within the ground-truth cell.
469 If several predicted cells are matched to a ground-truth cell, the number of surplus
470 matches is taken to be the number of segmentation errors. If no cells are matched to a
471 ground-truth cell, then the error is taken to be 1.

472

473 **Leveraging Omnipose to accelerate manual annotation**

474 Omnipose was periodically trained on our growing dataset to make initial cell
475 labels. These were converted into an N-color representation and loaded into Photoshop
476 for manual correction. A subset of our cytosol GFP channels were sufficient for training
477 Omnipose to segment based on fluorescence, and the resulting trained model enabled
478 higher-quality initial cell labels for GFP-expressing samples than could be achieved from
479 intermediate phase contrast models (e.g., *V. cholerae*).

480

481 Defining the Omnipose prediction classes

482 Omnipose predicts four classes: two flow components, the distance field, and a
483 boundary field. Our distance field is found by solving the eikonal equation

$$484 \quad |\vec{\nabla}\phi(\vec{x})| = \frac{1}{f(\vec{x})}$$

485 where f represents the speed at a point \vec{x} . The Godunov upwind discretization of the
486 eikonal equation is

$$487 \quad \left(\frac{\max(\phi_{i,j} - \min(\phi_{i-1,j}, \phi_{i+1,j}), 0)}{\Delta x} \right)^2 + \left(\frac{\max(\phi_{i,j} - \min(\phi_{i,j-1}, \phi_{i,j+1}), 0)}{\Delta y} \right)^2 = \frac{1}{f_{i,j}^2}$$

488 Our solution to this equation is based on the Improved FIM Algorithm 1.1 of (34),
489 as follows. Our key contribution to this algorithm is the addition of ordinal sampling to
490 boost both convergence and smoothness of the final distance field.

491 *2D update function for $\phi_{i,j}$ on a cartesian grid*

492 1. Find neighboring points for cardinal axes ($\Delta x = \Delta y = \delta$):

$$493 \quad \phi^{\min x} = \min(\phi_{i-1,j}, \phi_{i+1,j}), \quad \phi^{\min y} = \min(\phi_{i,j-1}, \phi_{i,j+1})$$

494 2. Find neighboring points for ordinal axes ($\hat{x} \cdot \hat{a} = \hat{y} \cdot \hat{b} = \frac{\sqrt{2}}{2}$, $\frac{\Delta a}{\Delta x} = \frac{\Delta b}{\Delta y} = \sqrt{2}\delta$):

$$495 \quad \phi^{\min a} = \min(\phi_{i-1,j-1}, \phi_{i+1,j+1}), \quad \phi^{\min b} = \min(\phi_{i+1,j-1}, \phi_{i-1,j+1})$$

496 3. Calculate update along cardinal axes:

$$497 \quad \text{if } |\phi^{\min x} - \phi^{\min y}| > \frac{\sqrt{2}\delta}{f_{i,j}}:$$

$$498 \quad U^{xy} = \min(\phi^{\min x}, \phi^{\min y}) + \frac{\delta}{f_{i,j}}$$

499 **else:**

$$500 \quad U^{xy} = \frac{1}{2} \left(\phi^{\min x} + \phi^{\min y} + \sqrt{2 \left(\frac{\delta}{f_{i,j}} \right)^2 - (\phi^{\min x} - \phi^{\min y})^2} \right)$$

501 4. Calculate update along ordinal axes:

502 **if** $|\phi^{\text{mina}} - \phi^{\text{minb}}| > \frac{2\delta}{f_{i,j}}$:

503
$$U^{ab} = \min(\phi^{\text{mina}}, \phi^{\text{minb}}) + \frac{\sqrt{2}\delta}{f_{i,j}}$$

504 **else:**

505
$$U^{ab} = \frac{1}{2} \left(\phi^{\text{mina}} + \phi^{\text{minb}} + \sqrt{4 \left(\frac{\delta}{f_{i,j}} \right)^2 - (\phi^{\text{mina}} - \phi^{\text{minb}})^2} \right)$$

506 5. Update with geometric mean:

507
$$\phi_{i,j} = \sqrt{U^{xy}U^{ab}}$$

508 This update rule is repeated until convergence (Fig. S5). We take $\delta = f_{i,j}$ to

509 obtain the signed distance field used in Omnipose. The flow field components are defined

510 by the normalized gradient of this distance field ϕ . The boundary field is defined by

511 points satisfying $0 < \phi < 1$. For network prediction, the boundary map is converted to

512 the logits (inverse sigmoid) representation, such that points in the range $[0,1]$ are mapped

513 to $[-5,5]$. For consistent value ranges across prediction classes, the flow components are

514 multiplied by 5 and all background values of the distance field ($\phi = 0$) are set to -5 .

515

516 **Omnipose network architecture**

517 The DNN used for Omnipose is a minor modification of that used in Cellpose: a

518 U-net architecture with two residual blocks per scale, each with two convolutional layers

519 (12). Omnipose introduces a dropout layer before the densely connected layer (56), which

520 we incorporated into the shared Cellpose and Omnipose architecture moving forward.

521 However, Cellpose models utilized in this study are trained without dropout.

522

523 **Rescaling flow field by divergence**

524 During training, the ground truth data is augmented by a random affine
525 transformation. The original implementation, and the one which yields the best results,
526 linearly interpolates the transformed field. This reduces the magnitude of the otherwise
527 normalized field in regions of divergence, *i.e.*, at boundaries and skeletons. A
528 renormalized field (obtained either from the transformed field or as the normalized
529 gradient of the transformed heat distribution) often has artifacts at cell boundaries and
530 skeletons, so the interpolated field effectively reduces the influence of these artifacts on
531 training. We reason that this feature explains the superior performance of interpolated
532 field training over renormalized fields, despite the latter being the nominal goal of the
533 algorithm.

534 Pixels at cell boundaries, however, consequently do not move far (less than 1px)
535 under Euler integration due to the low magnitude of the predicted field at cell boundaries.
536 Our solution in Omnipose is to rescale the flow field by the magnitude of the divergence.
537 The divergence is most positive at the cell boundaries (where pixels need to move) and
538 most negative at cell skeletons (where pixels need to stop). We therefore rescale the
539 divergence from 0 to 1 and multiply the normalized flow field by this new magnitude
540 map. This forces boundary pixels of neighboring cells to quickly diverge and allow for
541 accurate pixel clustering to obtain the final segmentation.

542

543 **Novel diameter metric**

544 The size models of Cellpose are trained to estimate the average cell ‘diameter’,
545 taken to be the diameter of the circle of equivalent area:

546
$$d = 2R = 2 \sqrt{\frac{A}{\pi}} \quad (*)$$

547 This metric as a basis for rescaling is problematic when cells are growing in
548 length but not width (Fig. S7D). Log-phase bacterial cell area grows exponentially with
549 time, and so too does the scale factor, eventually resulting in a rescaled image that is too
550 small for Cellpose to segment.

551 The average of the distance field, however, does not change for filamentous
552 bacteria, as the width – and therefore the distance to the closest boundary – remains
553 constant. To define a formula consistent with the previous definition in the case of a
554 circular cell, we consider mean of the distance field over the cell:

555
$$\bar{\phi} = \frac{1}{\pi R^2} \int_0^{2\pi} \int_0^R (R-r)r dr d\theta = \frac{1}{\pi R^2} \left(\frac{\pi}{3} R^3 \right) = \frac{R}{3}$$

556 This allows us to define a new ‘effective diameter’ as

557
$$d = 2R = 6\bar{\phi} \quad (**)$$

558 Aside from agreeing with the previous scaling method (*) for round
559 morphologies, this definition exhibits excellent consistency across time (Fig. S7C). This
560 consistency is also critical for training on datasets with wide distributions in cell areas
561 that require rescaling, such as the Cellpose datasets. Finally, the raw distance field output
562 of Omnipose can directly be used directly in (**) to estimate average cell diameter,
563 which is used in our code to automatically toggle on features that improve mask
564 reconstruction performance for small cells.

565

566 **Gamma augmentation**

567 To make the network robust against changes in exposure/contrast, the training
568 images are now raised to a random power (γ) between 0.5 and 1.25, simulating the
569 varying levels of contrast that are observed experimentally with different light sources,
570 objectives, and exposure times.

571

572 **Alleviating class imbalance**

573 Class imbalance remains a challenge in many machine learning applications (57).
574 In our dataset, foreground pixels (cells) take up anywhere from 1 to 75 percent of a given
575 training image, with the rest being background pixels that the network must only learn to
576 ignore (*i.e.*, assign a constant output of -5 for distance and boundary logits). We
577 implemented several changes to the loss function to emphasize foreground objects,
578 including weighting by the distance field and averaging some loss terms only over
579 foreground pixels. Our training augmentation function also attempts many random crop
580 and resizing passes until a field of view with foreground pixels is selected (this may take
581 several attempts for sparse images, but adds very little time to training).

582

583 **Image normalization**

584 To manage different image exposure levels, Cellpose automatically rescales
585 images such that pixels in the 1st percentile of intensity are set to 0 and those in the 99th
586 percentile are sent to 1. This percentile rescaling is preferred over blind min-max
587 rescaling because bubbles or glass can cause small bright spots in the image. However,
588 we found that images containing single cells (low intensity) in a wide field of media

589 (high intensity) would become badly clipped due to the foreground-background class
590 imbalance. To solve this, we changed the percentile range from 0.01 to 99.99.

591

592 **Data availability**

593 Ground truth images and labels generated for this study are available through the
594 paperswithcode database (<https://paperswithcode.com/>).

595

596 **Code availability**

597 Python and MATLAB scripts generated for this study is available from GitHub at
598 <https://github.com/kevinjohncutler/omnipose>. Omnipose is available as part of the
599 Cellpose package at <https://github.com/mouseland/cellpose>.

600 **Acknowledgements**

601 The authors wish to thank members of the Mougous and Wiggins laboratories for helpful
602 suggestions, Teresa Lo for assistance with image acquisition, Sophie Sichel and Nina
603 Salama lab for growing, fixing, and staining *H. pylori* samples for in-house imaging, and
604 David Kysela, Maxime Jacq and Yves Brun for providing *C. crescentus* images. This
605 work was supported by the NIH (AI080609 to JDM, GM128191 to PAW,
606 T32GM008268 to KJC). JDM is an HHMI Investigator.

607

608 **Competing interests**

609 The authors declare no competing interests.

610

611 **Author contributions**

612 KJC, PAW and JDM conceived the study. KJC performed experiments, analyzed data,
613 and wrote the code. KJC, PAW, and JDM wrote the manuscript. CS edited the
614 manuscript and assisted in code development.

615

616 **Author Information**

617 Correspondence and requests for materials should be addressed to J.D.M.
618 (mougous@u.washington.edu) or P.A.W. (pwiggins@uw.edu).

619

620 References

- 621 1. H. Jeckel, K. Drescher, Advances and opportunities in image analysis of bacterial
622 cells and communities. *FEMS Microbiol Rev* **45** (2021).
- 623 2. A. Bali, S. N. Singh (2015) A Review on the Strategies and Techniques of Image
624 Segmentation. in *IEEE Xplore* (IEEE), pp 113-120.
- 625 3. A. M. Lucas *et al.*, Open-source deep-learning software for bioimage
626 segmentation. *Mol Biol Cell* **32**, 823-829 (2021).
- 627 4. D. T. Kysela, A. M. Randich, P. D. Caccamo, Y. V. Brun, Diversity Takes Shape:
628 Understanding the Mechanistic and Adaptive Basis of Bacterial Morphology.
629 *PLoS Biol* **14**, e1002565 (2016).
- 630 5. S. E. Jones, M. A. Elliot, 'Exploring' the regulation of Streptomyces growth and
631 development. *Curr Opin Microbiol* **42**, 25-30 (2018).
- 632 6. P. D. Caccamo, Y. V. Brun, The Molecular Basis of Noncanonical Bacterial
633 Morphology. *Trends Microbiol* **26**, 191-208 (2018).
- 634 7. B. Behera *et al.*, Emerging technologies for antibiotic susceptibility testing.
635 *Biosens Bioelectron* **142**, 111552 (2019).
- 636 8. A. Paintdakhi *et al.*, Oufiti: an integrated software package for high-accuracy,
637 high-throughput quantitative microscopy analysis. *Molecular microbiology* **99**,
638 767-777 (2016).
- 639 9. A. Ducret, E. M. Quardokus, Y. V. Brun, MicrobeJ, a tool for high throughput
640 bacterial cell detection and quantitative analysis. *Nat Microbiol* **1**, 16077 (2016).
- 641 10. C. Tropini, K. A. Earle, K. C. Huang, J. L. Sonnenburg, The Gut Microbiome:
642 Connecting Spatial Organization to Function. *Cell Host Microbe* **21**, 433-442
643 (2017).
- 644 11. A. D. Balomenos *et al.*, Image analysis driven single-cell analytics for systems
645 microbiology. *BMC Syst Biol* **11**, 43 (2017).
- 646 12. C. Stringer, T. Wang, M. Michaelos, M. Pachitariu, Cellpose: a generalist
647 algorithm for cellular segmentation. *Nature methods* **18**, 100-106 (2021).
- 648 13. S. Stylianidou, C. Brennan, S. B. Nissen, N. J. Kuwada, P. A. Wiggins,
649 SuperSegger: robust image segmentation, analysis and lineage tracking of
650 bacterial cells. *Molecular microbiology* **102**, 690-700 (2016).
- 651 14. R. van Raaphorst, M. Kjos, J. W. Veening, BactMAP: An R package for
652 integrating, analyzing and visualizing bacterial microscopy data. *Molecular*
653 *microbiology* **113**, 297-308 (2020).

- 654 15. S. Panigrahi *et al.*, Mistic, a general deep learning-based method for the high-
655 throughput cell segmentation of complex bacterial communities. *Elife* **10** (2021).
- 656 16. D. Bannon *et al.*, DeepCell Kiosk: scaling deep learning-enabled cellular image
657 analysis with Kubernetes. *Nature methods* **18**, 43-45 (2021).
- 658 17. J. B. Lugagne, H. Lin, M. J. Dunlop, DeLTA: Automated cell segmentation,
659 tracking, and lineage reconstruction using deep learning. *PLoS computational*
660 *biology* **16**, e1007673 (2020).
- 661 18. J. H. Smit, Y. Li, E. M. Warszawik, A. Herrmann, T. Cordes, ColiCoords: A
662 Python package for the analysis of bacterial fluorescence microscopy data. *PLoS*
663 *One* **14**, e0217524 (2019).
- 664 19. E. Czech, B. A. Aksoy, P. Aksoy, J. Hammerbacher, Cytokit: a single-cell
665 analysis toolkit for high dimensional fluorescent microscopy imaging. *BMC*
666 *Bioinformatics* **20**, 448 (2019).
- 667 20. C. McQuin *et al.*, CellProfiler 3.0: Next-generation image processing for biology.
668 *PLoS Biol* **16**, e2005970 (2018).
- 669 21. S. Berg *et al.*, ilastik: interactive machine learning for (bio)image analysis. *Nature*
670 *methods* **16**, 1226-1232 (2019).
- 671 22. A. Wolny *et al.*, Accurate and versatile 3D segmentation of plant tissues at
672 cellular resolution. *Elife* **9** (2020).
- 673 23. T. Ursell *et al.*, Rapid, precise quantification of bacterial cellular dimensions
674 across a genomic-scale knockout library. *BMC Biol* **15**, 17 (2017).
- 675 24. H. F. Tsai, J. Gajda, T. F. W. Sloan, A. Rares, A. Shen, Usiigaci: Instance-aware
676 cell tracking in stain-free phase contrast microscopy enabled by machine learning.
677 *SoftwareX* **9**, 230-237 (2019).
- 678 25. J. Reiner, G. Azran, G. Hyams, MicroAnalyzer: A Python Tool for Automated
679 Bacterial Analysis with Fluorescence Microscopy. *arXiv*
680 <https://arxiv.org/abs/2009.12684> (2020).
- 681 26. U. Schmidt *et al.*, *Cell Detection with Star-Convex Polygons*, Medical Image
682 Computing and Computer Assisted Intervention -- MICCAI 2018 (2018),
683 https://link.springer.com/chapter/10.1007/978-3-030-00934-2_30, pp. 265-273.
- 684 27. K. He, G. Gkioxari, P. Dollar, R. Girshick, Mask R-CNN. *arXiv*
685 <https://arxiv.org/abs/1703.06870> (2018).
- 686 28. K. Shal, M. S. Choudhry, Evolution of Deep Learning Algorithms for MRI-Based
687 Brain Tumor Image Segmentation. *Crit Rev Biomed Eng* **49**, 77-94 (2021).

- 688 29. G. J. Bean *et al.*, A22 disrupts the bacterial actin cytoskeleton by directly binding
689 and inducing a low-affinity state in MreB. *Biochemistry* **48**, 4852-4857 (2009).
- 690 30. R. F. Laine, I. Arganda-Carreras, R. Henriques, G. Jacquemet, Avoiding a
691 replication crisis in deep-learning-based bioimage analysis. *Nature methods* **18**,
692 1136-1144 (2021).
- 693 31. A. A. Taha, A. Hanbury, Metrics for evaluating 3D medical image segmentation:
694 analysis, selection, and tool. *BMC Med Imaging* **15**, 29 (2015).
- 695 32. W. Lu *et al.*, Unsupervised Sequential Outlier Detection With Deep Architectures.
696 *IEEE Trans Image Process* **26**, 4321-4330 (2017).
- 697 33. J. A. Sethian, A. Vladimirsky, Ordered upwind methods for static Hamilton-
698 Jacobi equations. *Proc Natl Acad Sci U S A* **98**, 11069-11074 (2001).
- 699 34. Y. Huang, Improved Fast Iterative Algorithm for Eikonal Equation for GPU
700 Computing. *arXiv* <http://arXiv:2106.15869v3> (2021).
- 701 35. M. Ester, H. P. Kriegel, J. Sander, X. Xu, A density-based algorithm for
702 discovering clusters in large spatial databases with noise. 10.1.1.121.9220 (1996).
- 703 36. S. Y. Ting *et al.*, Bifunctional Immunity Proteins Protect Bacteria against FtsZ-
704 Targeting ADP-Ribosylating Toxins. *Cell* **175**, 1380-1392 (2018).
- 705 37. J. A. Cusick, C. L. Wellman, G. E. Demas, The call of the wild: using non-model
706 systems to investigate microbiome-behaviour relationships. *J Exp Biol* **224**
707 (2021).
- 708 38. Z. Wang, Cell Segmentation for Image Cytometry: Advances, Insufficiencies, and
709 Challenges. *Cytometry A* **95**, 708-711 (2019).
- 710 39. C. He *et al.*, Genome-resolved metagenomics reveals site-specific diversity of
711 episymbiotic CPR bacteria and DPANN archaea in groundwater ecosystems. *Nat*
712 *Microbiol* **6**, 354-365 (2021).
- 713 40. S. Looi (2019) rotated_maskrcnn. (GitHub).
- 714 41. R. Bharti, D. G. Grimm, Current challenges and best-practice protocols for
715 microbiome analysis. *Brief Bioinform* **22**, 178-193 (2021).
- 716 42. W. K. Smits, O. P. Kuipers, J. W. Veening, Phenotypic variation in bacteria: the
717 role of feedback regulation. *Nat Rev Microbiol* **4**, 259-271 (2006).
- 718 43. J. Bailey *et al.*, Essential gene deletions producing gigantic bacteria. *PLoS*
719 *genetics* **15**, e1008195 (2019).

- 720 44. J. A. Cass, S. Stylianidou, N. J. Kuwada, B. Traxler, P. A. Wiggins, Probing
721 bacterial cell biology using image cytometry. *Molecular microbiology* **103**, 818-
722 828 (2017).
- 723 45. B. M. Meberg, F. C. Sailer, D. E. Nelson, K. D. Young, Reconstruction of
724 *Escherichia coli* mrcA (PBP 1a) mutants lacking multiple combinations of
725 penicillin binding proteins. *J Bacteriol* **183**, 6148-6149 (2001).
- 726 46. A. C. Lowenthal *et al.*, Functional analysis of the *Helicobacter pylori* flagellar
727 switch proteins. *J Bacteriol* **191**, 7147-7156 (2009).
- 728 47. J. A. Taylor *et al.*, Distinct cytoskeletal proteins define zones of enhanced cell
729 wall synthesis in *Helicobacter pylori*. *Elife* **9** (2020).
- 730 48. M. Evinger, N. Agabian, Envelope-associated nucleoid from *Caulobacter*
731 *crescentus* stalked and swarmer cells. *J Bacteriol* **132**, 294-301 (1977).
- 732 49. P. D. Caccamo, M. Jacq, M. S. VanNieuwenhze, Y. V. Brun, A Division of Labor
733 in the Recruitment and Topological Organization of a Bacterial Morphogenic
734 Complex. *Curr Biol* **30**, 3908-3922 e3904 (2020).
- 735 50. N. Robertson, D. P. Sanders, P. Seymour, R. Thomas, A new proof of the four-
736 colour theorem. *Electron. Res. Announc. Amer. Math. Soc.*
737 <https://doi.org/10.1090/S1079-6762-96-00003-0> (1996).
- 738 51. S. Stylianidou, C. Brennan, S. B. Nissen, N. J. Kuwada, P. A. Wiggins,
739 SuperSegger: robust image segmentation, analysis and lineage tracking of
740 bacterial cells. *Molecular microbiology* **102**, 690–700 (2016).
- 741 52. R. Hartmann, M. C. F. van Teeseling, M. Thanbichler, K. Drescher, BacStalk: A
742 comprehensive and interactive image analysis software tool for bacterial cell
743 biology. *Molecular microbiology* **114**, 140-150 (2020).
- 744 53. A. Goni-Moreno, J. Kim, V. de Lorenzo, CellShape: A user-friendly image
745 analysis tool for quantitative visualization of bacterial cell factories inside.
746 *Biotechnol J* **12** (2017).
- 747 54. J. W. Young *et al.*, Measuring single-cell gene expression dynamics in bacteria
748 using fluorescence time-lapse microscopy. *Nature protocols* **7**, 80-88 (2011).
- 749 55. O. M. O'Connor, R. N. Alnahhas, J. B. Lugagne, M. J. Dunlop, DeLTA 2.0: A
750 deep learning pipeline for quantifying single-cell spatial and temporal dynamics.
751 *bioRxiv* <https://doi.org/10.1101/2021.08.10.455795> (2021).
- 752 56. N. Srivastava, G. Hinton, A. Krizhevsky, I. Sutskever, R. Salakhutdinov,
753 Dropout: a simple way to prevent neural networks from overfitting. *The Journal*
754 *of Machine Learning Research* **15**, 1929-1958 (2014).

- 755 57. H. Kaur, H. S. Pannu, A. K. Malhi, A Systematic Review on Imbalanced Data
756 Challenges in Machine Learning: Applications and Solutions. *ACM Computing*
757 *Surveys* **52**, 1-36 (2019).
- 758 58. B. M. Meberg, F. C. Sailer, D. E. Nelson, K. D. Young, Reconstruction of
759 *Escherichia coli* mrcA (PBP 1a) mutants lacking multiple combinations of
760 penicillin binding proteins. *J Bacteriol* **183**, 6148–6149 (2001).
- 761 59. V. Barbe *et al.*, Unique features revealed by the genome sequence of
762 *Acinetobacter* sp. ADP1, a versatile and naturally transformation competent
763 bacterium. *Nucleic Acids Res* **32**, 5766-5779 (2004).
- 764 60. Y. Yu *et al.*, Genomic patterns of pathogen evolution revealed by comparison of
765 *Burkholderia pseudomallei*, the causative agent of melioidosis, to avirulent
766 *Burkholderia thailandensis*. *BMC microbiology* **6**, 46 (2006).
- 767 61. A. Allue-Guardia, M. Echazarreta, S. S. K. Koenig, K. E. Klose, M. Eppinger,
768 Closed Genome Sequence of *Vibrio cholerae* O1 El Tor Inaba Strain A1552.
769 *Genome Announc* **6** (2018).
- 770 62. C. K. Stover *et al.*, Complete genome sequence of *Pseudomonas aeruginosa*
771 PA01, an opportunistic pathogen. *Nature* **406**, 959–964 (2000).
772

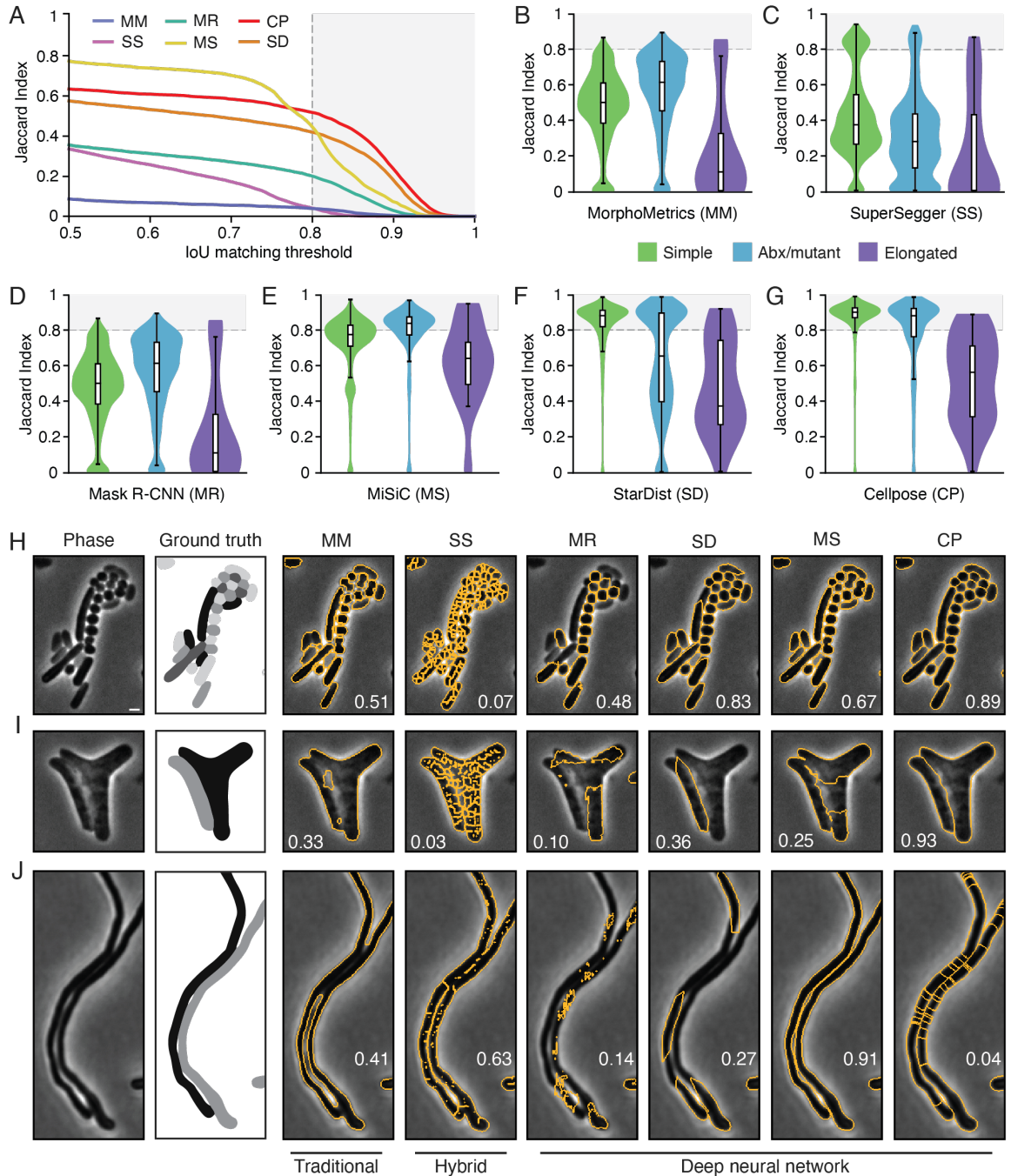


Figure 1. Quantitative comparison of segmentation methods distinguishes Cellpose as a high performing algorithm. (A-G) Comparison of segmentation algorithm performance on our test dataset. (A) Overall performance measured by Jaccard Index (JI). The JI was calculated at the image level and values averaged across the dataset are displayed. Algorithm abbreviations defined in B-G. (B-G) Algorithm performance partitioned by cell type (Simple, $n=12,869$; Abx/mutant, $n=6,138$; Elongated, $n=46$). Images were sorted into types as defined in Supplemental Table 1 (Abx, antibiotic). (H-J) Representative micrographs of cell type partitions analyzed in B-G, indicated by vertical bars at right. Ground-truth masks and predicted mask outlines generated by the indicated algorithm are displayed. Mean matched IoU values for cells shown are displayed within each micrograph. Bacteria displayed are (H) *Vibrio cholerae*, *Pseudomonas aeruginosa*, *Bacillus subtilis*, *Staphylococcus aureus*, (I) aztreonam-treated *Escherichia coli* CS703-1, and (J) *Streptomyces pristinaespiralis*. All images scaled equivalently; scale bar is 1mm.

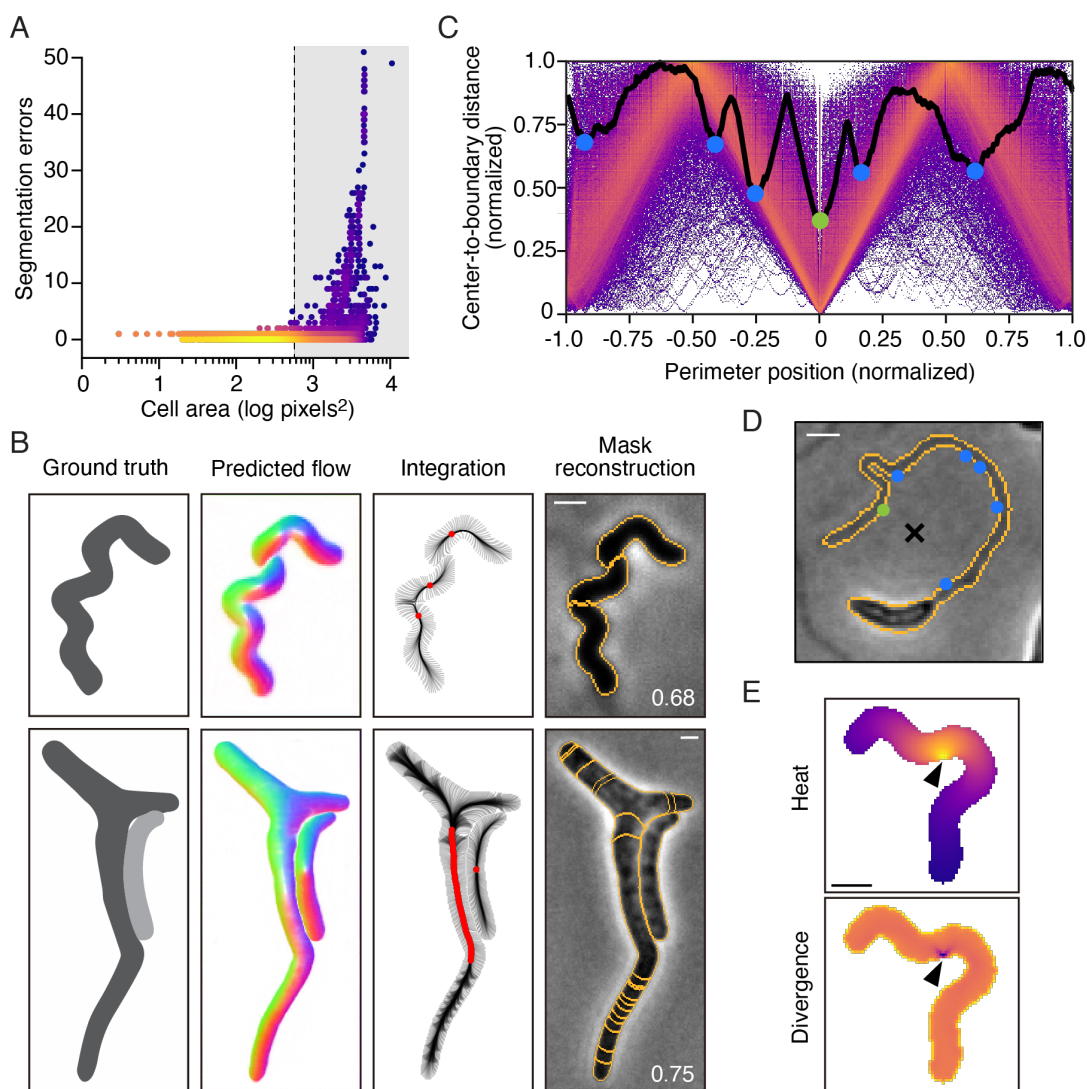


Figure 2. Cellpose over-segments extended, anisotropic cells. **(A)** Single-cell analysis of segmentation error as a function of cell area. Color represents density on a log scale. Gray box represents the top quartile of cell areas. **(B)** Representative examples exhibiting problematic flow fields. Corresponding boundary pixel trajectories are shown in black and final pixel locations in red. Predicted mask overlays are shown with mean matched IoU values. **(C)** Analysis of stochastic center-to-boundary distances. Distance from the center (median pixel coordinate) to each boundary pixel is normalized to a maximum of 1. Position along the boundary is normalized from -1 to 1 and centered on the point closest to the median pixel. Center-to-boundary for the cell in panel D is highlighted in black. **(D)** Representative cell with median coordinate outside the cell body (black X). Cellpose projects this point to the global minima of this function (green dot), but several other local minima exist (blue dots). **(E)** The heat distribution resulting from a projected cell center (black arrow). The normalized gradient corresponds to the divergence shown. Scale bars are 1 μm .

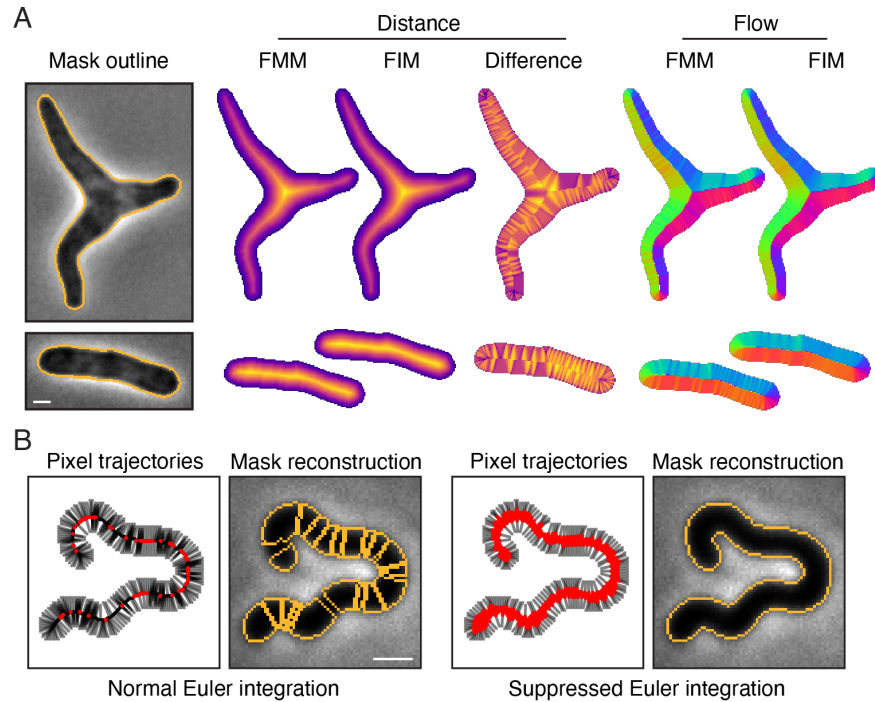


Figure 3. Core innovations of Omnipose. **(A)** Comparison of distance field algorithms and corresponding flow fields. Fast Marching Method (FMM) produces ridges in the distance field resulting from pixelation on the cell mask boundary. Our smooth FIM algorithm minimizes these features. The difference image (FIM – FMM) highlights artifacts in the FMM method. Flow fields are calculated as the normalized gradient of the distance field. Boundary pixelation affects the FMM flow field deep into the cell, regardless of cell size. **(B)** Comparison of mask reconstruction algorithms on a smooth flow field (not shown). Left: boundary pixel trajectories and resulting mask outlines from standard Euler integration. Right: Trajectories and mask outlines under suppressed Euler integration. Red dots indicate the final positions of all cell pixels, not only the boundary pixels for which trajectories are displayed. Scale bars are 1 μm .

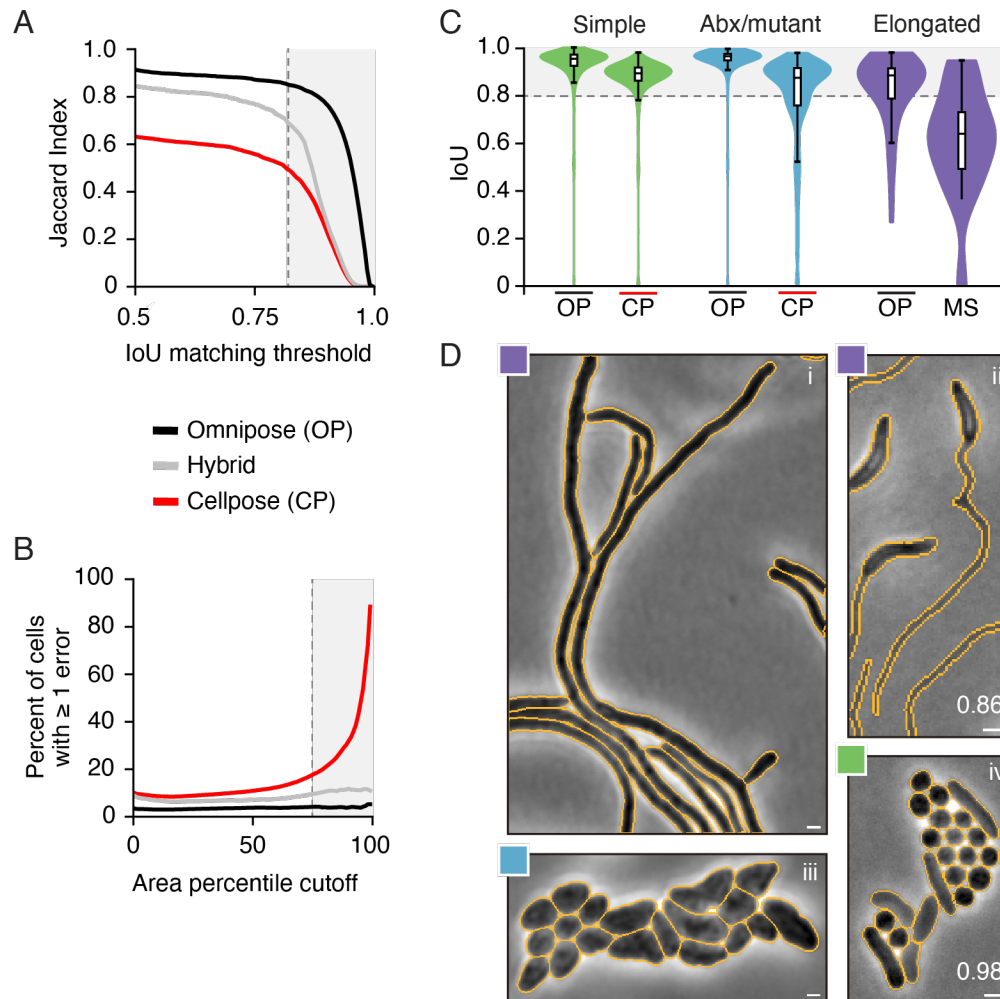


Figure 4. Omnipose outperforms Cellpose. **(A)** Omnipose IoU distribution on our dataset compared to the next highest performing algorithm in each of three cell categories. **(B)** Example micrographs and Omnipose segmentation. Mean matched IoU values shown. **(C)** Overall performance measured by Jaccard Index (JI). The hybrid method (gray) is a variant of Cellpose that uses the original center-seeking flow output and the mask reconstruction of Omnipose. Gray box represents $\text{IoU} \geq 0.8$. **(D)** Quantification of segmentation performance by cell size. The percent of cells with at least one segmentation error is computed for cells in each area percentile group from 1 to 100. Gray box represents the top quartile. Scale bars are 1 μm .

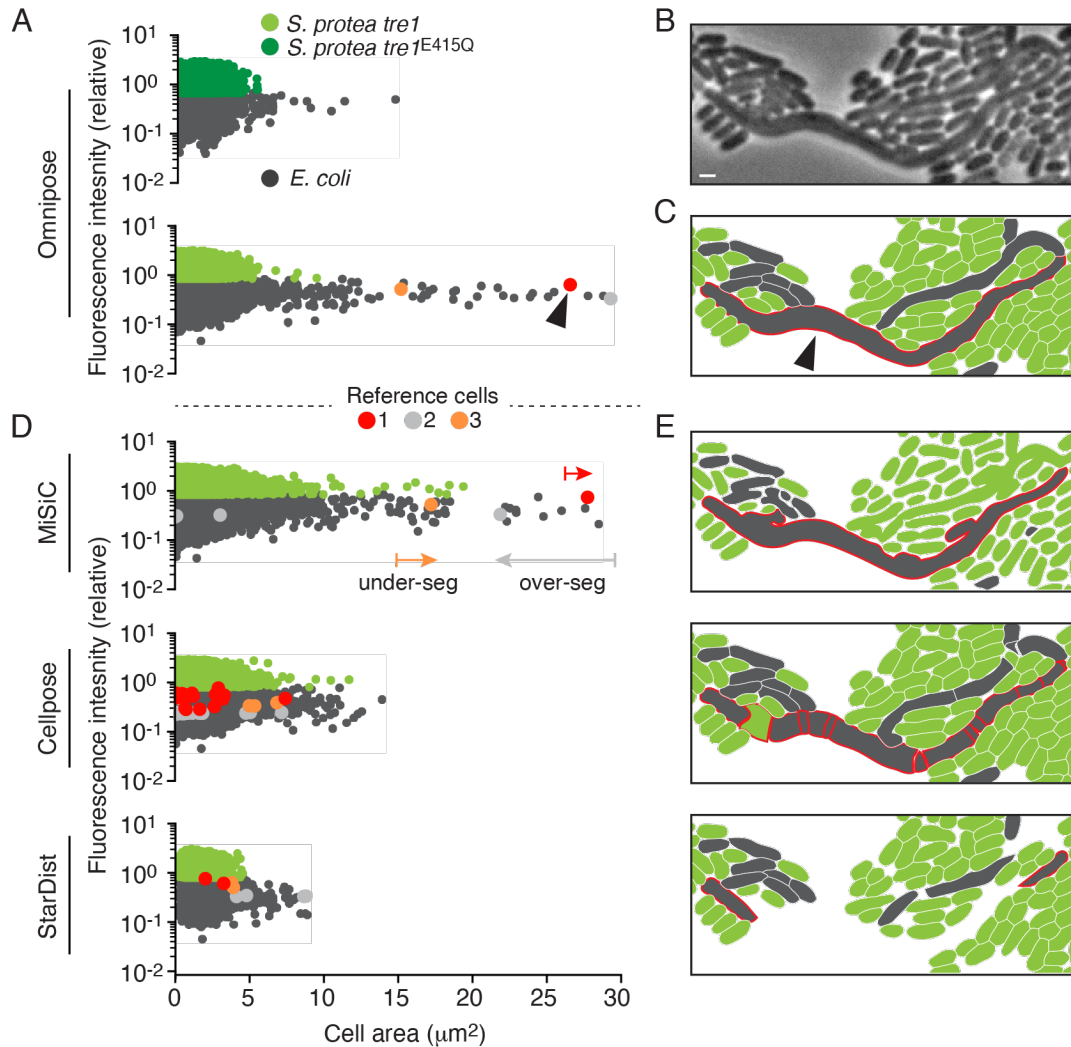


Figure 5. Sensitive detection of a toxin-induced morphological phenotype. (A) Fluorescence/area population profile according to Omnipose segmentation in control and experimental conditions. K-means clustering on GFP fluorescence distinguishes *S. proteamaculans tre1/tre1^{E415Q}* (light/dark green markers) from *E. coli* (gray markers). (B) Example of extreme filamentation of *E. coli* in response to active Tre1. (C) Omnipose accurately segments all cells in the image. Largest cell indicated with black arrow. (D) MiSiC predicts large cell masks over both species. Cellpose and StarDist fail to predict any cells above 15μm². (E) Example segmentations show that MiSiC masks are not single-cell accurate. Cellpose over-segments long cells and under-segments neighboring cells. StarDist predicts incomplete cell masks. Mask mergers cause some *E. coli* to be misclassified as *S. protea*. Scale bar is 1 μm.

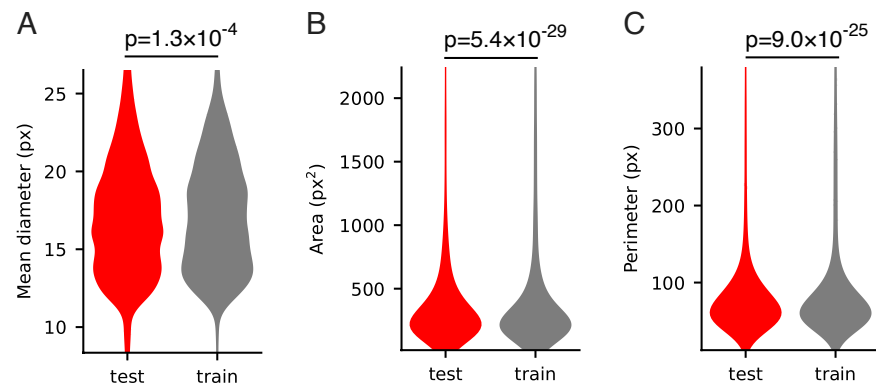


Figure S1. Test dataset is representative of the training dataset. (A) Mean diameter, defined in Methods. (B) Cell area. (C) Cell perimeter. P-values are displayed for the two-sided KS test.

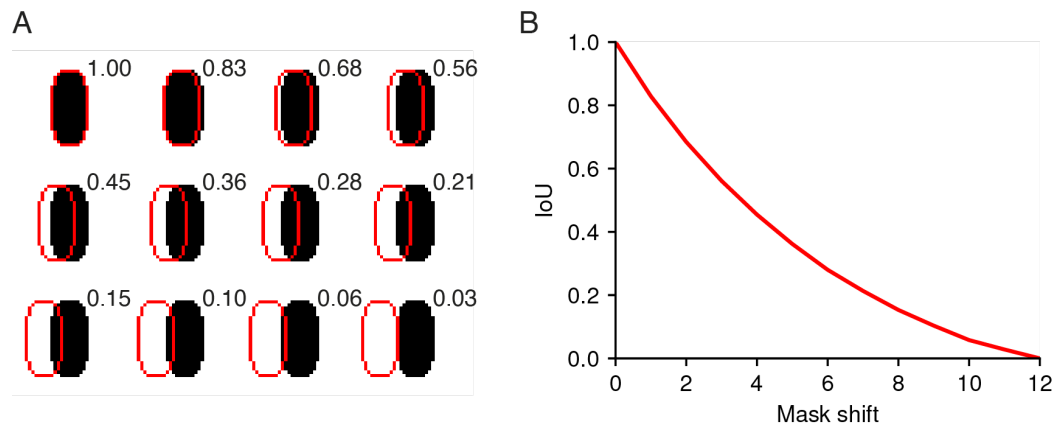


Figure S2. IoU values for synthetic cell of typical size/resolution. **(A)** 0-12 pixel displacement of cell mask (red outline) and corresponding IoU values. **(B)** IoU decreases non-linearly for curved regions such as this synthetic cell.

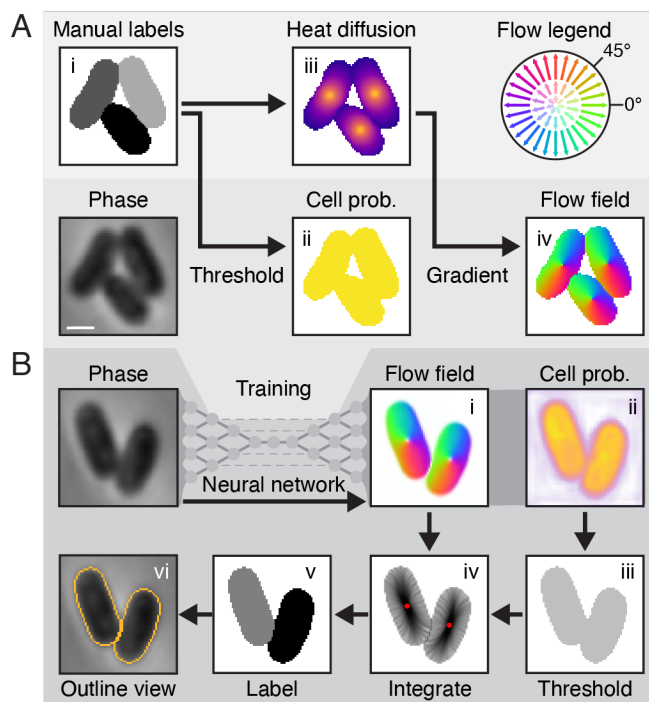


Figure S3. Details of the Cellpose algorithm. **(A)** Stages of the Cellpose training pipeline. Ground truth masks (*i*) are converted to cell probability (*ii*) by binary thresholding and a heat distribution (*iii*) by simulated diffusion from the median pixel coordinate. The flow field (*iv*) is defined by the normalized gradient of (*iii*). Color-magnitude representations of this vector field follow the flow legend diagram. The phase, cell probability, and flow fields are used to train the network. **(B)** Stages of the cellpose prediction pipeline. Phase images are processed by the trained cellpose network into the intermediate flow field and cell probability outputs (*i-ii*). A binary threshold is applied to the probability to identify cell pixels (*iii*). Pixels are Euler-integrated under the flow field until they converge at common points. Boundary pixel trajectories are depicted in *iv*. Each pixel is assigned a unique label corresponding to the center to which it converged (*v*). This segmentation result is commonly depicted in an outline view (*vi*). Scale bar is 1 μm .

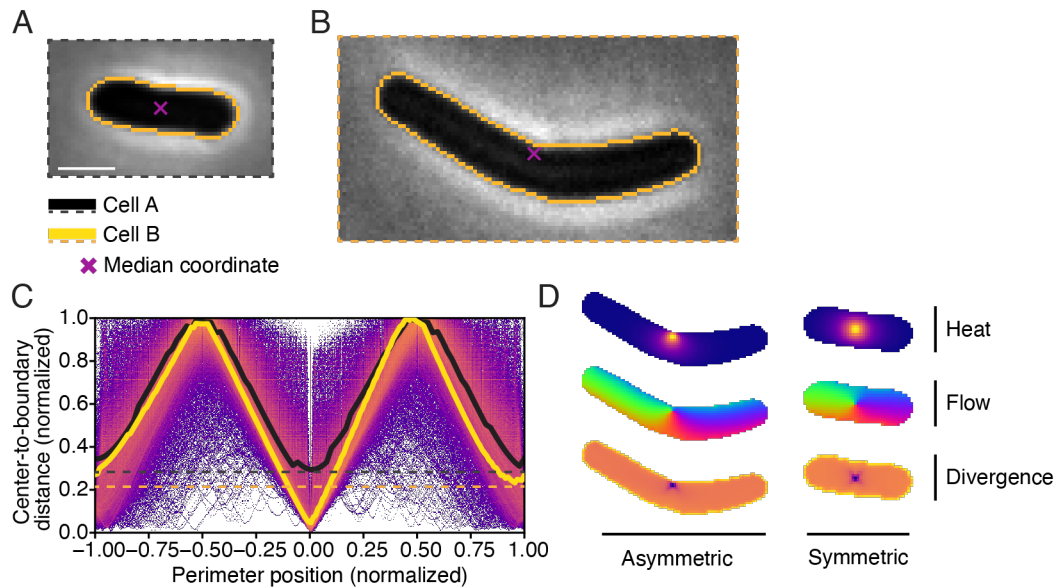


Figure S4. Median coordinates are asymmetrically localized. **(A)** Center-to-boundary distance highlighted for two cells with non-projected median coordinates. Dashed lines indicate the larger of the two minima along the medial axis. **(B)** Rod-shaped *E. coli* with symmetric median coordinate. Symmetry of the center is reflected in A by equal high and low points corresponding to the extremal points along the long and short axes of the cell. **(C)** Curved *B. subtilis* with median coordinate asymmetrically close to the cell boundary. This asymmetry is reflected in A by a secondary minimum above the global minimum corresponding to the diametrically opposing point along the short axis of the cell. **(D)** These centers result in distinct flow fields reflecting the (a)symmetry of the cell center. Scale bar is 1 μm . Images scaled equivalently.

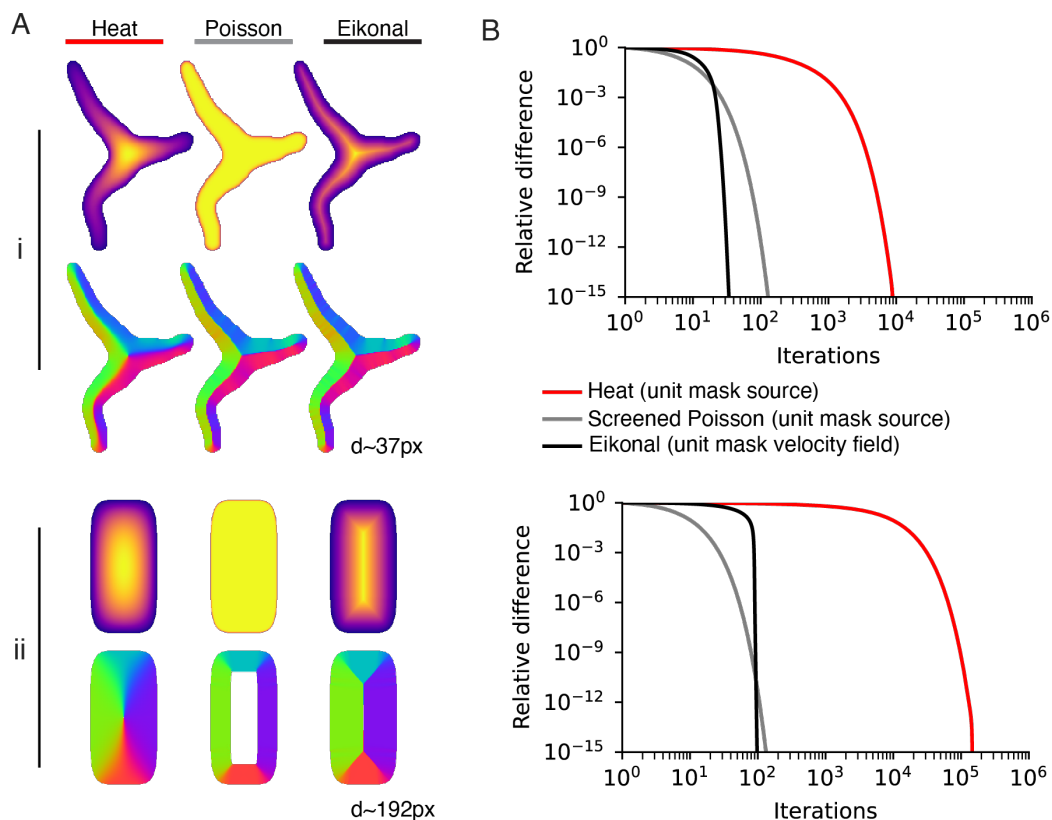


Figure S5. Comparison of three algorithms for computing center-independent flow fields. Each is defined by a partial differential equation with the mask at the source: time-independent heat equation, the screened Poisson equation, and the Eikonal equation. We solve these equations with iterative relaxation (see Methods). **(A)** Two example cells, the first drawn from our dataset with a mean diameter of 37px and a synthetic rod-shaped cell with a mean diameter of 192px. Cell (i) exhibits heat-derived flow components pointing toward the skeleton near boundaries and toward the global cell center at the skeleton. Center-seeking flow components become problematic for mask reconstruction for more complicated cell geometries, namely those with oscillating thickness. The screened Poisson and Eikonal equations produce nearly identical flow fields (same direction, normalized magnitude). Cell (ii) reveals a core flaw in the screened Poisson solution: its derivative exceeds our available numerical precision, leading to a vanishing flow field at the center where the solution plateaus. Any cells of this size or larger will exhibit this issue. **(B)** Convergence measured by the average difference at each iteration (maximum normalized to 1) for cells (i,ii). Our Eikonal solution converges faster than the other methods by a wide margin at typical cell diameters (i).

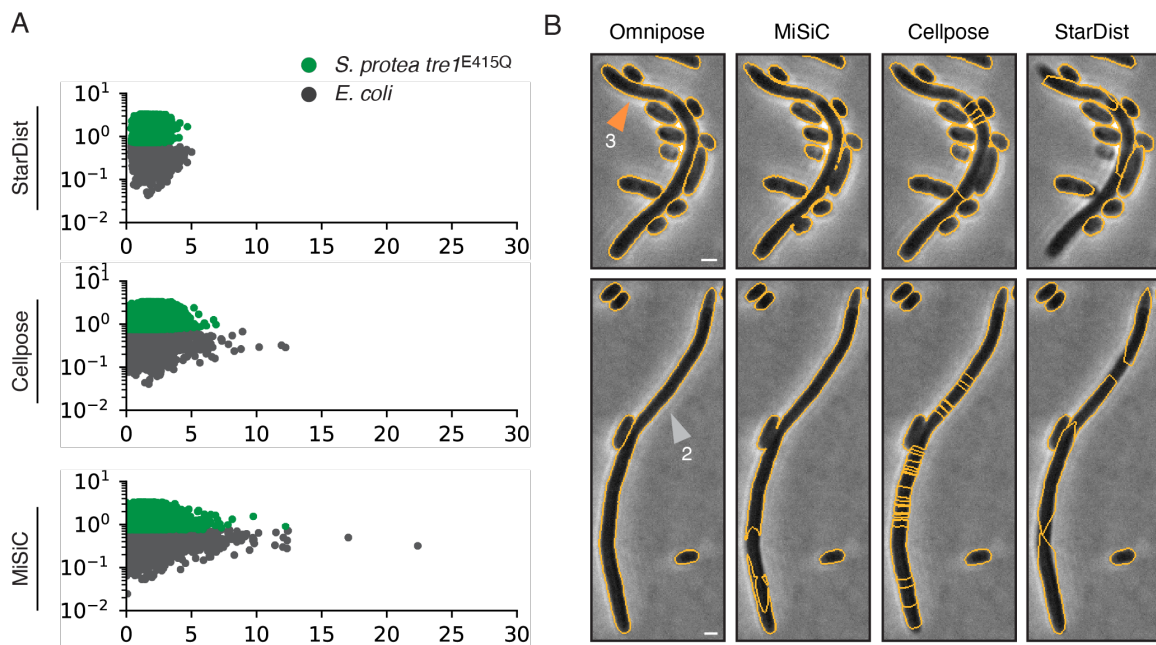


Figure S6. Controls and additional examples. **(A)** Controls segmented by StarDist, Cellpose, and MiSiC. Notably, Cellpose and MiSiC exhibit an enrichment of larger cells even in the control, a consequence of both under-segmented (merged) cells as well as fragments of over-segmented large cells. **(B)** Cells 2 and 3 highlighted in orange and gray plotted in Fig. 5A,D. Scale bars are 1 μm .

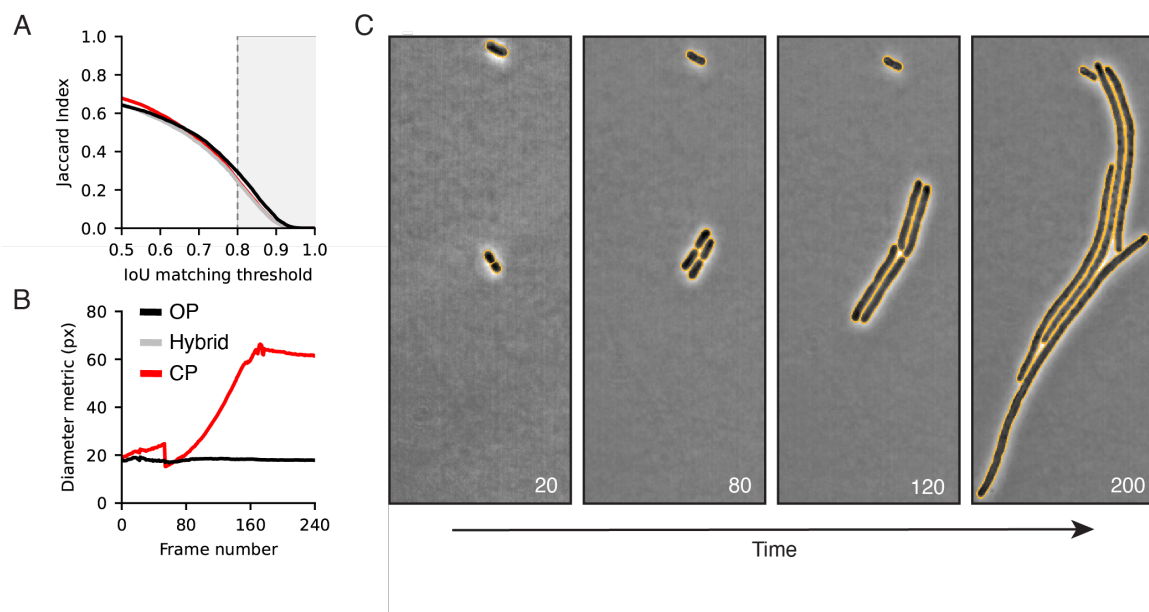


Figure S7. Omnipose can be applied to non-bacterial datasets. **(A)** Performance of Omnipose on the cyto2 dataset. **(B-C)** Comparison of diameter metrics on a mutant bacterial microcolony. Scale bar is 1 μm .

Supplemental Table 1.

Species	Strain	Image count	Cell Count	Cells in GT	Percent of GT	Notes
<i>Escherichia coli</i>	DH5a	1378	98200	9733	20.6	Dense microcolonies grown on minimal media. Thin phenotype. ITPG-induced GFP cytosol marker. Time lapse. Imaged by the Wiggins lab.
		141	4536	4395	9.3	Dense microcolonies on LB. Time lapse. Imaged by the Wiggins lab.
		2	2277	-	-	Treatment with cephalixin. Tn7::GFP. Imaged by the Mougous lab.
	CS703-1 (58)	80	23169	1299	2.6	Mutant grown on LB and aztreonam. Elongated and branching phenotypes. Time lapse. Imaged by the Mougous lab.
<i>Shigella flexneri</i>	M90T	117	256618	1409	3.0	Treatment with A22. Tn7::GFP. Frames selected from time lapse after 1hr growth. Imaged by the Mougous lab.
		6	4482	4318	9.2	Treatment with cephalixin. Tn7::GFP. Frames selected from time lapse after 1hr growth. Imaged by the Mougous lab.
<i>Francisella tularensis subsp. novicida</i>	U112	5	20166	496	1.1	Small and extremely low-contrast cells. Tn7::GFP. Imaged by the Mougous lab.
<i>Acinetobacter baylyi</i>	ADP1 (59)	2169	60601	3336	7.1	Deletion of essential gene <i>murA</i> . Rounded phenotype. Time lapse. Imaged by the Wiggins lab.
		241	1313	1133	2.4	Deletion of essential gene <i>ftsN</i> . Filamentous phenotype. Time lapse. Imaged by the Wiggins lab.
		540	10013	2227	4.7	Deletion of essential gene <i>dnaA</i> . Filamentous phenotype. Time lapse. Imaged by the Wiggins lab.
<i>Burkholderia thailandensis</i>	E264 (60)	30	62005	5122	10.9	Selected panels from a self-intoxication experiment. Cells exhibit internal structure and low contrast in microcolonies. Tn7::GFP. Time lapse. Imaged by the Mougous lab.
<i>Helicobacter pylori</i>	LHS100 (46)	15	13014	-	-	Helical phenotype. Grown, fixed, and stained with Alexaflour 488 in the lab of

						Nina Salama. Imaged by the Mougous lab.
		19	1668	701	1.5	Treated with aztreonam. Filamentous, helical phenotype. Grown, fixed, and stained with Alexafluor 488 in the lab of Nina Salama. Imaged by the Mougous lab.
<i>Caulobacter crescentus</i>	NA1000 (48)	4	1787	756	1.6	Grown on low phosphate media to induce stalk phenotype. Cultivation and imaging done in the lab of Yves Brun.
<i>Streptomyces pristinaespiralis</i>	NRRL 2958	17	2339	270	0.6	Grown on rich media to induce filamentous phenotype. Imaged by the Mougous lab.
<i>Vibrio cholerae</i>	A1552 (61)	2	2627	2265	4.8	Cells have short but curved morphology and form dense, low-contrast microcolonies. Tn7::GFP. Obtained from the lab of Fitnat Yildiz. Imaged in the Mougous lab.
<i>Serratia proteamaculans</i> <i>E. coli</i>	568 DH5 α	43	100146	1244	2.6	1:1 mixture. <i>S.p.</i> labelled via Tn7::GFP, <i>E.c.</i> unlabeled. Time lapse. Imaged in the Mougous lab.
<i>Pseudomonas aeruginosa</i> <i>Staphylococcus aureus</i>	PAO1 (62) USA300	3	2662	3688	7.8	1:1 mixture. <i>P.a.</i> labelled via Tn7::GFP, <i>S.a.</i> unlabeled. Imaged in the Mougous lab.
<i>P. aeruginosa</i> <i>S. aureus</i> <i>V. cholerae</i> <i>Bacillus subtilis</i>	PAO1 USA300 A1552 HM1350	21	33281	4678	9.9	1:1:1:1 mixture. <i>P.a.</i> and <i>V.c.</i> labelled via Tn7::GFP, <i>S.a.</i> and <i>B.s.</i> labelled with red membrane dye. Imaged in the Mougous lab.
		4833	700904	47070	100	